10.2514/6.2015-3506

International Space Planes and Hypersonic Systems and Technologies Conferences
6-9 July 2015, Glasgow, Scotland
20th AIAA International Space Planes and Hypersonic Systems and Technologies Conference

An Approach to Computing the Combustion Efficiency of a Scramjet-Powered Hypersonic Vehicle

Chukwuka C. Mbagwu*, James F. Driscoll†

Combustion efficiencies of a hypersonic vehicle were computed for different combustor pressures and temperatures using a reduced-order model called MASIV (Michigan AFRL scramjet in vehicle). This is a joint effort between the University of Michigan and AFRL. The 3-D turbulent mixing and combustion process in the combustor is simulated with 3-D empirical relations that were measured for fuel jets injected into a cross flow along with finite rate flamelet chemistry computations. The 3-D results are reduced to 1-D lookup tables and are interpolated using a POD method. The computations quantify the loss in combustion efficiency caused by operating at low combustion pressure and the gain achieved by operating at higher combustor inlet temperature. The method also provides a way to determine how much improvement in combustion efficiency is gained by increasing the number of fuel port injectors.

Nomenclature

S_b	=	burning velocity [m/s]
U_g	=	incoming gas velocity [m/s]
U_F	=	fuel jet velocity [m/s]
f_s	=	stoichiometric mixture fraction
S_T	=	turbulent burning velocity [m/s]
S_L	=	stretched laminar burning velocity [m/s]
S_L/S_{L0}	=	non-dimensional stretch factor
Ka	=	Karlovitz number
α_0	=	thermal diffusivity
u'_g	=	turbulence level of gas at flame base
h	=	liftoff height [m]
d_F	=	fuel jet diameter [m]
p_3	=	pressure at combustor inlet [Pa]
T_3	=	temperature at combustor inlet [K]
U_3	=	velocity entering the combustor [m/s]
Da	=	Damkohler number

I. Introduction

The Bolender-Doman AFRL model of hypersonic aircraft [1] was reported in 2007, and it has been used in several studies to predict flight dynamics, control strategies, and the effects of vehicle bending [2–4]. For example, Parker et al. [2] used the AFRL model of a generic vehicle to show how the poles and zeros of the flight dynamics depend on the flight Mach number; their results suggested that an additional control surface, namely a canard, should be added. Skujins et al. [3] and Oppenheimer et al. [4] demonstrated that the as the aircraft bends, the location of the bow shock wave moves, and this changes the spillage of the air that bypasses the engine, which affects the thrust. The Bolender-Doman AFRL model is a first-principles reduced-order model, which means that the fundamental conservation equations are solved, but certain 2-D and 1-D assumptions are made in order to reduce the complexity of the problem. For example, since the vehicle is slender, they applied conventional piston theory to compute aerodynamic forces. Their engine flow was assumed to be one-dimensional, the bow shock was assumed to be 2-D, and they ignored any shock waves downstream of the bow shock. Reduced-order models also have been used for aircraft design by O'Neill and Lewis [5] and Bowcutt [6]. McQuade et al. [7] developed a different type of reduced-order model that reduces the number of CFD (Computational Fluid Dynamics) runs required to optimize the design of a hypersonic aircraft. Mor and Livne [8] optimized the trajectory of a reentry vehicle and developed a new way to simultaneously optimize the vehicle shape and size. Dalle and Torrez have improved the Bolender-Doman AFRL model in order to avoid some of the assumptions that were made in the original model [9–12]. Recently they have developed methodology required to compute both the engine unstart and the ram-scram transition boundaries for a trimmed waverider vehicle [11]. The

*Graduate Research Assistant, Department of Aerospace Engineering, AIAA Member, cmbagwu@umich.edu
†Professor, Department of Aerospace Engineering, AIAA Fellow, jamesfd@umich.edu

improved model is called the MASTrim (Michigan/ AFRL Scramjet Trim) code.

The MAX-1 vehicle geometry was selected to be similar to the generic aircraft that was first considered by Bolender and Doman [1]. Its length is 29.1 m (95.4 ft), and the inlet to the dualmode ramjet-scramjet engine is rectangular with a sufficiently large aspect ratio of 15.3 such that it can be considered two-dimensional. The approach of the AFRL program has been to maintain the same geometry but to make gradual improvements to make it more realistic. The size of the control surfaces were optimized [2], the weight distribution was altered [4], and aeroelastic properties were added [2, 4].

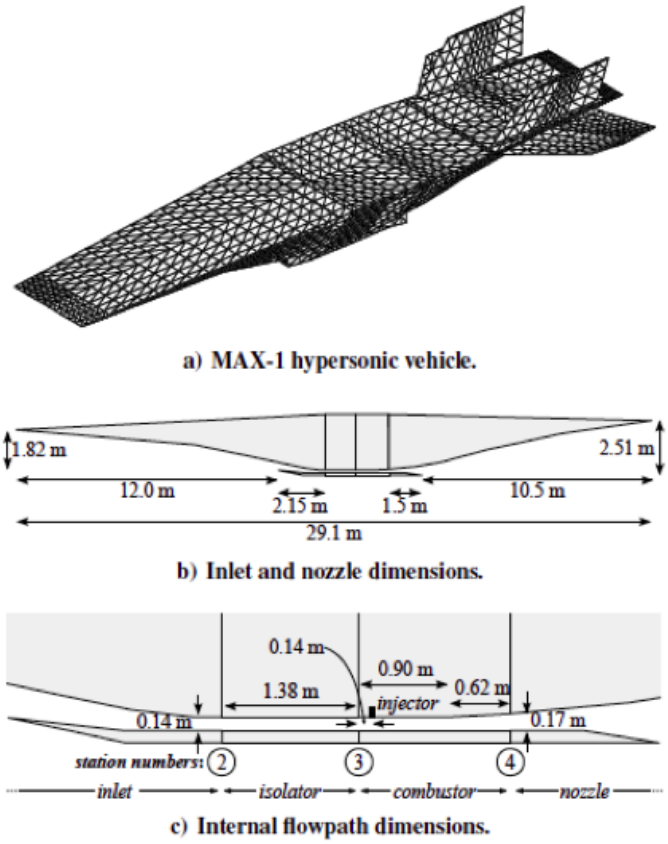

Figure 1. MAX-1 vehicle and flow path dimensions. Engine width is 2.143 m.

In the present effort, the properties of hydrogen-air combustion were computed using the Stanford FLAMEMASTER code, which includes full kinetics. It considers non premixed flamelets within a turbulent flame and it solves the flamelet equations. From these solutions we obtain lookup tables that relate the chemical reaction rate of major species to the local fuel-air ratio (mixture fraction). The MASIV code computes the local fuel-air ratio and then the lookup tables provide rapid mapping of the reaction rates to the (x,y,z) location in the engine.

To rapidly access the chemistry lookup tables, a mathematical method called proper orthogonal decomposition (POD) is used. POD is a well-defined method of producing reduced-order, but very accurate, models of large or complex data sets. It has been used in computational fluid dynamics (CFD) analysis to examine correlations of the structure of turbulent flowfields in time [13–15]. Other time-domain applications include constructing reduced-order models (ROM) of cylinder vortex shedding [16] and an aeroelastic model of a two-dimensional airfoil [17]. Analogous frequency-domain POD techniques have been explored by Kim [18], applied to a spring damper system and three-dimensional vortex lattice model. ROMs constructed using POD have been combined with structural dynamic models and applied to aeroelastic systems [19, 20]; it has also been found effective for flutter analysis [21, 22]. It has also been used for reduced-order models of atmospheric and oceanographic data, where the control space is high-dimensional [23].

In this work, the application of POD techniques to reduce multidimensional flamelet chemistry data used in a model for the mixing and combustion of turbulent jets in crossflow is discussed. A brief overview of POD theory is given, and those methods are applied to the flamelet data in the turbulent reacting flow. The advantages and scalability

of this technique are explored, and select comparisons are made of the full-order, non-reduced flamelet model to that of the results of the POD analysis.

Finally, using the preceding POD architecture, various thermal properties and combustion efficiencies are calculated over a wide range of combustor operating conditions. As a hypersonic vehicle travels upward along an ascent trajectory, the static pressure in the scramjet combustor will decrease, which can lead to engine flameout. At low pressures the chemical reactions between the fuel and air become excessively slow. However, during the ascent the flight Mach huber is increasing; this increases the stagnation temperature and the static temperature at the combustor entrance, tending to prevent flameout. These trends are observed and provide insight to determine flameout limits and ultimately flight trajectory envelopes for a hypersonic vehicle. Such results using simple and reduced models prove useful for rapid design and trajectory optimization.

A. The Hypersonic Vehicle Engine Model (MASIV)

MASIV is a control-oriented reduced-order model for the propulsion system of a hypersonic vehicle. It is an advanced version of the AFRL model. It solves the following seven ordinary differential equations, which include the conservation of mass, momentum, energy, and species.

The isolator model of Heiser and Pratt [26] is used to relate the pressure rise, separated boundary layer size, and exit Mach number. They derived the following relation using the equations for conservation of mass and momentum across the isolator assuming that the shock train separates the flow into two separate streams: the central core flow and the low-speed separated boundary layer.

1. Thermal Choking

In the ram mode the downstream boundary condition is that the local Mach number is unity at the thermal choking location, xC. Shapiro [32] describes the general method to determine xC. He explains that a singularity occurs and an application of L'Hospital's rule yields a condition for xC that must be met to ensure that the flow can be solved through the singularity. The resulting condition is that

II. Proper Orthogonal Decomposition (POD) Method of Approximating MASIV Flamelet Tables

The combustion flamelet data used in MASIV are stored in large, multi-dimensional structures. In particular, the gas reaction rates are found in 3-D lookup tables for each gas species that contain the rate data for discrete permutations of mixture fraction f, mixedness s, and scalar dissipation χ. Currently, data is retrieved through an interpolation of the function along the table near the given dimensions. Proper Orthogonal Decomposition (POD) presents a method of approximating the function with a linear combination of basis functions, which affords the same data to be reconstructed from a smaller data set and less storage space.

Consider a model where a vector $\mathbf{u}_j$ is calculated at J discrete points within some domain for $j = 1, 2, \ldots, J$. The $\mathbf{u}_j$ vector may consist of P quantities of interest as shown in equation (1).

For a two-dimensional inviscid flow problem, one might choose a vector $\mathbf{u}_j$ where $P = 4$ and the states are density, x-momentum, y-momentum, and energy. But in general, $\mathbf{u}_j$ may contain any type of information for points P. In this work $\mathbf{u}_j = \dot{\omega}_j$, the reaction rate for a single species as a function of several flamelet reference variables, as described in Section III.

Combining the solution vectors $\mathbf{u}_j$ over the domain of J points, we end up with a column vector of the form

$$\mathbf{u}_j = \begin{pmatrix} u_{j,1} \\ \vdots \\ u_{j,P} \end{pmatrix}, \qquad \mathbf{q}^m = \begin{pmatrix} \mathbf{u}_1 \\ \vdots \\ \mathbf{u}_J \end{pmatrix} \tag{1}$$

where $\mathbf{q}^m$ is a snapshot of the configuration for $m = 1, 2, \ldots, M$. Continuing the example of the inviscid CFD problem, m can be chosen to be snapshots in time. However, m may generally be any parameter or configuration affecting the solutions at each of the J points.

The goal of POD is to represent all of the data approximately using a linear combination of $K \leq M$ basis vectors ϕ_k. These vectors are much like snapshots, but are not in general equal to any individual snapshots. Linearly combining the M snapshots yields

$$\phi_k = \sum_{m=1}^{M} \mathbf{q}^m v_k^m = \mathbf{S}\mathbf{v}_k \Longleftrightarrow \Phi = \mathbf{S}\mathbf{V} \tag{2}$$

where $\mathbf{v}_k = \left(v_k^1, v_k^2, \cdots, v_k^M\right)^T$ and each entry is the contribution of the mth snapshot to the kth basis vector. Φ is a matrix of dimension $J \times K$ such that each colum is a basis vector ϕ_k. $\mathbf{S}$ is a matrix of dimension $J \times M$ such that each column is a snapshot $\mathbf{q}^m$. $\mathbf{V}$ is a matrix of dimension $M \times K$ such that each column is $\mathbf{v}_k$.

Hall et al. [27] shows that this result reduces to an eigenvalue problem of the form

$$\mathbf{S}\mathbf{S}^H\mathbf{S}\mathbf{v}_k = \lambda_k \mathbf{S}\mathbf{v}_k \tag{3}$$

where $\mathbf{S}^H$ is the Hermitian or conjugate transpose of $\mathbf{S}$. Solving for the eigenvalues λ_k provides a correlation between the eigenvectors $\mathbf{v}_k$ and the basis vectors ϕ_k. The eigenvectors with the largest values of λ_k contribute the most to the values of ϕ_k.

Rathinam and Petzold [28] explore the corollary for representing data sets in a general real space $\mathbb{R}^n$, using a subspace $\mathbb{S} \subset \mathbb{R}^n$. Here, POD minimizes the total square distance of the former data set to the projected data on $\mathbb{S}$, and $\mathbb{S}$ corresponds to the subspace determined by largest eigenvalues of the system.

A. POD On Flamelet Chemistry Data

The reduced-order mixing model examined in this work is part of the MASIV architecture, which is a complete flow model developed at the University of Michigan for a hypersonic vehicle with specified geometry and gas properties. It is further described in Torrez et al. [10] The mixing ROM incorporates the pressure, temperature, mean mixture fraction f, mixture fraction variance s, and the scalar dissipation rate χ of various gas species to determine the reaction rates throughout the combustion process and subsequently solve the 1D conservation equations. The reaction rate of each species varies with the aforementioned parameters, and those parameters are functions of the spatial variables in the vehicle combustor and isolator. As a result, multiple chemistry tables must be generated and stored to capture the reaction rate behavior for the wide range of pressures, temperatures, scalar dissipation rates, and species. The chemistry tables are then interpolated to find the particular reaction rate at a given location and condition.

Following the formulation described in Section II, the solution vector, or quantity of interest, $\mathbf{u}_j$ is set to be the reaction rate at the jth value of the lookup variables. The mean mixture fraction and variance parameters are bounded between 0 and 1, so the j-values are chosen to be discrete combinations of f and s, respectively. The data sets contain $n_1 = 201$ discrete mean mixture fraction points and $n_2 = 25$ mixture fraction variance points, creating $J = n_1 n_2 = 5025$ combinations of the aforementioned lookup variables. Therefore, one snapshot of the solution $\mathbf{q}^m$ in configuration m is defined as

$$\mathbf{u}_j = u_j = \dot{\omega}_j, \qquad \mathbf{q}^m = \begin{pmatrix} \dot{\omega}_1 \\ \vdots \\ \dot{\omega}_{5025} \end{pmatrix}, \qquad \mathbf{S} = \left(\mathbf{q}^1, \cdots, \mathbf{q}^M\right) \tag{4}$$

This snapshot is graphically shown in Figure 1, for a given configuration. $\mathbf{S}$ is then a row vector of the M snapshots. For the simplest case in this work, these snapshots are chosen to be $M = 46$ scalar dissipation rates at a fixed temperature and pressure for one species.

Discrete methods of POD are analogous to a matrix decomposition called singular value decomposition [29], which is a common mathematical tool implemented on many computational platforms, and is used for this analysis. Any matrix $\mathbf{S}$ can be written as the product

$$\mathbf{S} = \mathbf{U}\Sigma\mathbf{W}^H \tag{5}$$

where $\mathbf{U}, \mathbf{W}$ are unitary matrices of size J and M, respectively. Σ is a $J \times M$ matrix where the diagonal entries $\sigma_m = \sqrt{\lambda_m}$ are the square roots of the eigenvalues of $\mathbf{S}^H\mathbf{S}$, and are the only nonzero entries. For discrete POD analysis, we propose choosing a correlation quantity $0 < \Gamma \leq 1$ and setting K as the smallest integer such that

$$\sum_{k=1}^{K} \sigma_k / \sum_{m=1}^{M} \sigma_m \geq \Gamma, \qquad K \leq M \tag{6}$$

for the Σ matrix. The determination of a satisfying K value subsequently yields the basis functions for the approximation as described in Section I. An analogous approach for the general real space example in [28] defines a *correlation*

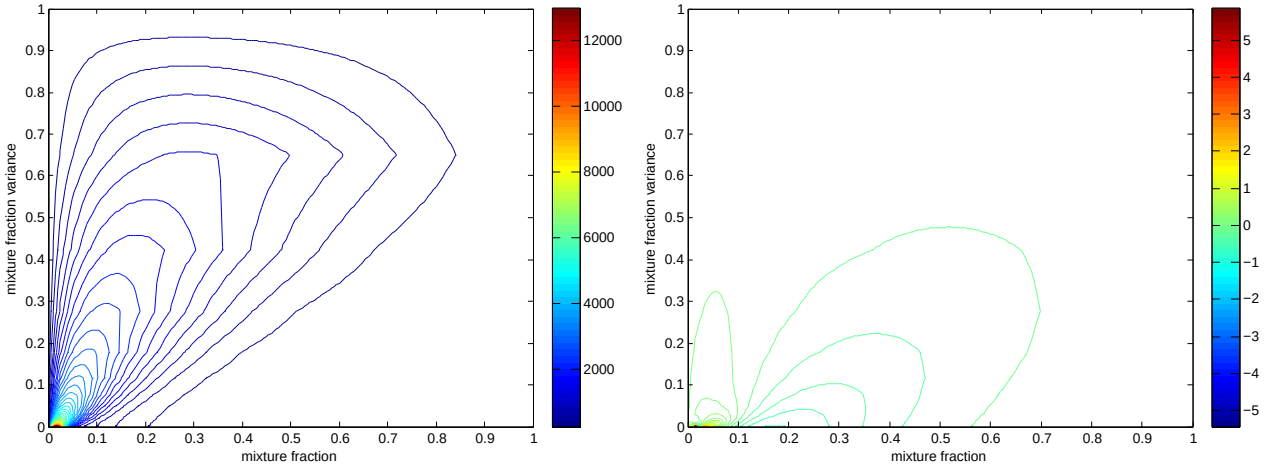

a) Contours of Reaction Rate **b) Contours of Reaction Rate Error**

Figure 2. Flamelet conditions: H2O at p = 2.61 bar, T = 1280 K, and χ = 312.3 [1/s].

matrix from which the eigenvalues are determined. A similar procedure is followed in [23] for producing this matrix to compute the eigenvalues.

For this application, we look to the simplest case of taking the snapshots $\mathbf{q}^m$ of the $\mathbf{S}$ matrix in equation (4) to be a range of $M = 46$ scalar dissipation rates for a single species, H_2O, at a fixed pressure and temperature. The correlation quantity is set to be $(1 - \Gamma) = 10^{-3}$. Decomposing $\mathbf{S}$ and satisfying the condition in equation (6) for Σ, one finds that $K = 4$.

We create three new matrices: $\tilde{\Sigma} = diag\left(\sigma_1, \cdots, \sigma_{K=4}\right)$, with all other entries being zero, and $\tilde{\mathbf{U}}, \tilde{\mathbf{W}}$ as the $(J \times 4)$ and $(M \times 4)$ parts of the $\mathbf{U}$ and $\mathbf{W}$ matrices, respectively. These three matrices approximate the function of the entire table with only a fraction of the data and storage. By multiplying $\tilde{\mathbf{U}}, \tilde{\Sigma}$, and $\tilde{\mathbf{W}}$ according to equation (5) we can recover a new data set $\tilde{\mathbf{S}}$, which is an accurate approximation of $\mathbf{S}$. A comparison of $\mathbf{S}$ and $\tilde{\mathbf{S}}$ for the same snapshot is shown in Figure 2.

The fractional savings can be measured by comparing the number of data points in the decomposition to that of the full set:

$$\delta = \frac{(J \times K) + (K \times K) + (K \times M)}{(J \times M)} \times 100\% \tag{7}$$

For this example of H_2O at $p = 2.61$ bar and $T = 1280$ K, we find that $\delta = 8.78\%$. This shows that a small percentage of the data can be retained, while still capturing nearly all of characteristics of the reaction rate behavior over the domain.

B. Additional Input Dimensions to the POD Approximation

The POD analysis may be extended to account for additional parameters on which the reaction rate depends. In Section III, the gas species, pressure, and temperature were specified such that the only variable parameter outside of the J points of mixture fraction/variance was the scalar dissipation rate. The range of the scalar dissipation rates made up the M snapshots. Say that we are now interested in the reaction rates for N number of species. We must then obtain tabulated data for the matrix $\mathbf{S}^n$ given in equation (4) for each of the N species. Defining a new matrix $\mathbf{S}_{total}$, a concatentation of the $\mathbf{S}$ matrices, we get

$$\mathbf{S}_{total} = \left(\mathbf{S}^1, \cdots, \mathbf{S}^N\right) \tag{8}$$

Introducing additional dimensions to the data follows the same procedure. Allowing pressure as a variable will require the result in equation (8) to be tabulated at each pressure. Accounting for temperature variation again multiplies the size of the resulting matrix by the number of temperature points, and so on. Thus, the general $\mathbf{S}_{total}$ matrix will be of the form:

$$\mathbf{S}_{total} = \Big[\underbrace{\overbrace{\underbrace{\mathbf{q}^1, \cdots, \mathbf{q}^M}_{\mathbf{S}^1}, \cdots, \mathbf{S}^N}^{\mathbf{S}^1_N}, \cdots, \mathbf{S}^R_N, \cdots, \mathbf{S}^V_{N,R}, \cdots}_{\mathbf{S}^1_{N,R}} \Big] \tag{9}$$

for additional dimensions with number of points M, N, R, V, . . . , respectively. Note that while the total number of snapshots $\mathbf{q}^{M\times N\times R\times V\times\cdots}$ increases with the added dimensions, the number of $J = 5025$ points remains the same.

Table 1 compares the results of POD for increasing numbers of snapshots and dimensions, for the same correlation quantity $(1 - \Gamma) = 10^{-3}$.

Table 1. Scaling POD to Higher Dimensional Data Sets

Varying Parameters	# Data Points	# Basis	Fraction δ
None (1) - no reduction	5025	1	100%
× Scalar Dissipation (46)	231150	4	8.78%
× Species (8)	1849200	8	2.34%
× Pressures (4)	7396800	10	0.75%

The information here shows that POD is highly effective in approximating multidimensional data sets, while only adding few eigenvalues/basis functions for each new parameter and using a smaller fraction of the total data.

C. Model Accuracy

To determine the accuracy of the POD approximation, we compare the original data set $\mathbf{S}$ to the recovered data set $\tilde{\mathbf{S}} = \tilde{\mathbf{U}}\tilde{\Sigma}\tilde{\mathbf{W}}^H$ after the matrix decomposition and eigenvalue analysis. Integrating the absolute error of the reaction rate at each point in the matrices is an insufficient approach, as larger data sets will inevitably sum to larger total errors. Instead, we look to match the aggregate properties of both data sets, the mean, variance, and standard deviation, and infer the accuracy of the approximation from their likeness. Table 2 shows the percent difference of the root-mean-square $(\tilde{\mu}, \mu)$, variance $(\tilde{\nu}, \nu)$, and standard deviation $(\tilde{\sigma}, \sigma)$ of the approximated data set $\tilde{\mathbf{S}}$ with respect to $\mathbf{S}$, for each case discussed in Section IV.

Table 2. Mean, Variance, and Standard Deviation Error

Varying Parameters	$(\tilde{\mu}/\mu - 1)$	$(\tilde{\nu}/\nu - 1)$	$(\tilde{\sigma}/\sigma - 1)$
None (1) - no reduction	-3.8×10^{-8}	5.8×10^{-5}	2.9×10^{-5}
× Scalar Dissipation (46)	-8.8×10^{-8}	8.0×10^{-6}	4.0×10^{-6}
× Species (8)	-9.2×10^{-8}	-1.8×10^{-7}	-9.2×10^{-8}
× Pressures (4)	-8.5×10^{-8}	-1.7×10^{-7}	-8.5×10^{-8}

The results show that even while the size of the data increases significantly with each added dimension, the aggregate behavior of the reaction rate for both the original data set and the POD approximation remain strongly correlated. It is important, however, to recognize that this is not necessarily true for the general case. It is possible to construct data sets such that the matrix $\mathbf{S}$ becomes ill-conditioned and the eigenvalue analysis produces less accurate basis vectors. In such cases, POD is not sufficient and other methods must be used for a better approximation.

We can see that for this application, using POD to reduce and approximate large flamelet chemistry data sets proves to be very effective and accurate. Where the multidimensionality of the reaction rate requires numerous chemistry tables to be generated, POD is most useful in reducing the storage and memory footprint, while maintaining the integrity of the data with low error margins. This allows those computational resources to be allocated elsewhere in the reduced-order model. If not all of the data is needed, the relevant portions can be recovered by combining only parts of the decomposition, eliminating the wasted storage of keeping the full chemistry tables. Recovering the full data set is easily done by multiplying the full matrices from the decomposition.

IV. Combustor Operation at Varying Conditions

Typical scramjet engine notation designates station 3 as the entrance to the vehicle combustor. Multiple sets of initial conditions are run through the combustor while enforcing the appropriate gas and species conservation laws. The fuel-oxidizer mixing mechanism is computed via a reduced order model of the 3-D mixing and 3-D turbulent combustion processes of a jet in a supersonic cross flow. This model is described by Torrez et. al. The starting conditions are prescribed as follows:

$T_3 = 1300K \equiv$ combustor inlet temperature (same as lookup table)
$\phi = 0.3 \equiv$ equivalence ratio
$u_3 = 2000m/s \equiv$ combustor inlet velocity

and P_3, the combustor inlet pressure, is varied logarithmically between 0.1 and 3.16 bar. A separate chemistry lookup table was generated for each pressure value.

A. Resulting Thermal Properties

Figure 1 shows the variation of pressure and temperature across the vehicle combustor.

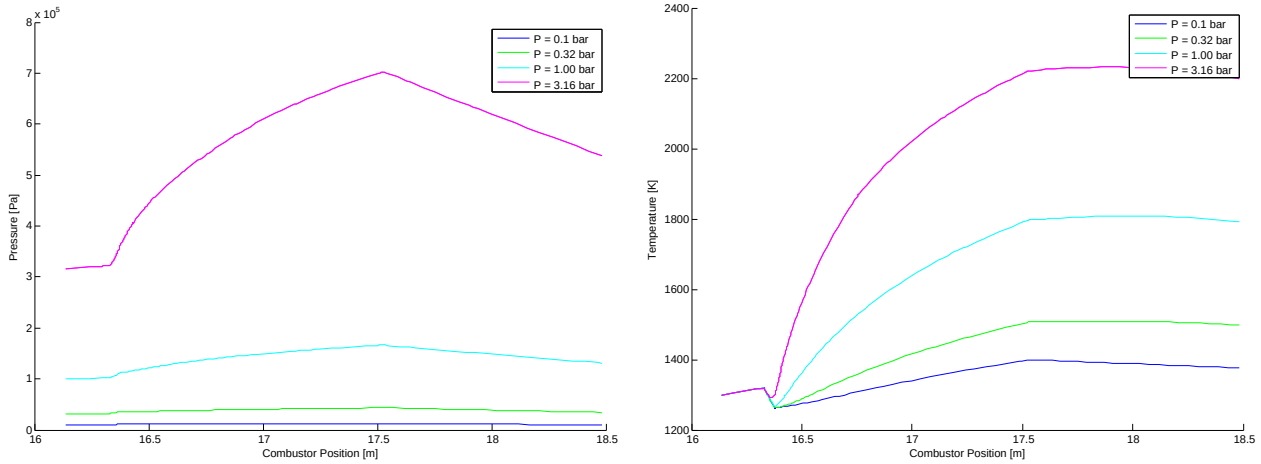

a) Pressure **b) Temperature**

Figure 3. Flow properties along the length of the combustor.

The reaction rates of the key chemical species H_2, the primary fuel, and H_2O, the main reaction product and determinant of overall efficiency, are highly sensitive to the incoming pressure (and temperature) conditions. Figure 2 implies an optimal pressure condition in the vicinity $P = 1$ bar that maximizes fuel burn.

Combustion efficiency is determined by the mass fraction of H_2O of the reaction products. In the case of the mixing-limited scramjet combustion, we measure the efficiency from as far downstream the engine as possible according to equation (11):

$$\eta_c \equiv \frac{Y_{H_2O}(x)}{Y_{H_2O_{ideal}}} = \frac{Y_{H_2O}(x = x_4)}{Y_{H_2O_{ideal}}} \tag{20}$$

where $Y_{H_2O_{ideal}}$ is defined in equation (7) as the H_2O mass fraction in a fully burned stoichiometric reaction, and x_4 is the location at the end of the combustor.

An alternative measure of combustion efficiency lies in the corollary to previous formulation. Instead of measuring the reaction products generated to determine efficiency, we can also look at the depletion of the combustion reactants. In particular, for complete combustion we expect the mass fraction of the fuel H_2 to go to zero. Combustion efficiency can thus be formulated as follows:

$$\eta_c = 1 - \frac{Y_{H_2}(x = x_4)}{Y_{H_2}(x = o^+)} \tag{21}$$

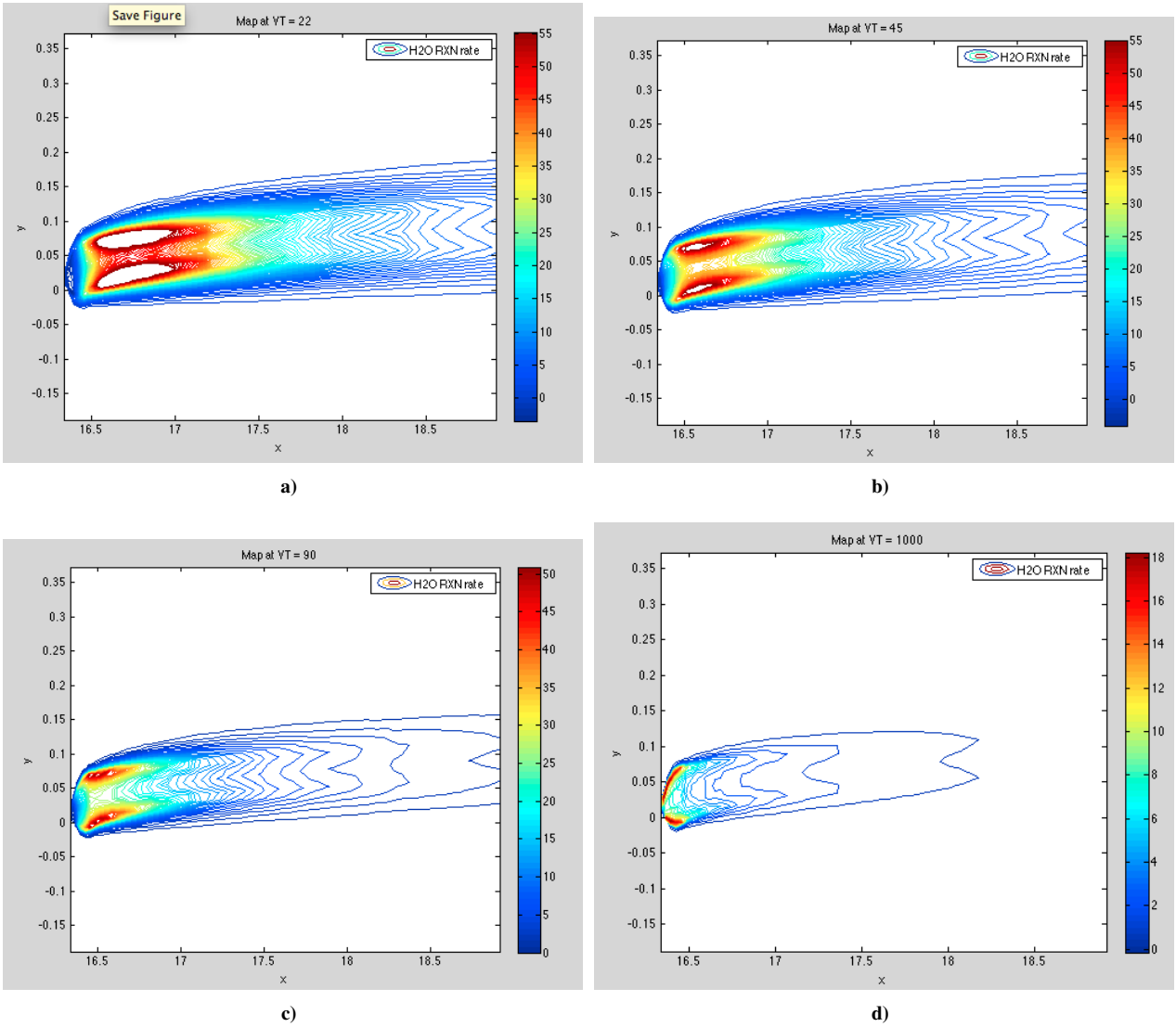

Figure 4. Three dimensional contours of H2O reaction rate computed using MASIV above the wall port where fuel is injected (x = 16.5 cm). Air flow is left to right.

V. Results

Figure 4 shows the computed contours of the H2O reaction rate above the fuel port where the hydrogen fuel is injected into the air stream. As expected, the mixing and chemical reaction rate is most intense just above the fuel port (x = 16.5 cm) and it becomes smaller downstream where the fuel is nearly all consumed. These profiles were computed by using the empirical formulas for the mean mixture fraction in a jet in a cross flow, as explained in Ref. 10. The empirical formulas show that the centerline of the jet bends over and its height (y) above the bottom wall is proportional to the streamwise distance (x) to the one-third power. Then the mixture fraction at each (x, y, z) location is used to compute a mixture fraction gradient from which the fluctuations in mixture fraction is computed, along with the local dissipation rate. These values are converted into a chemical reaction rate using the POD interpolation of the chemistry tables, as described in section II.

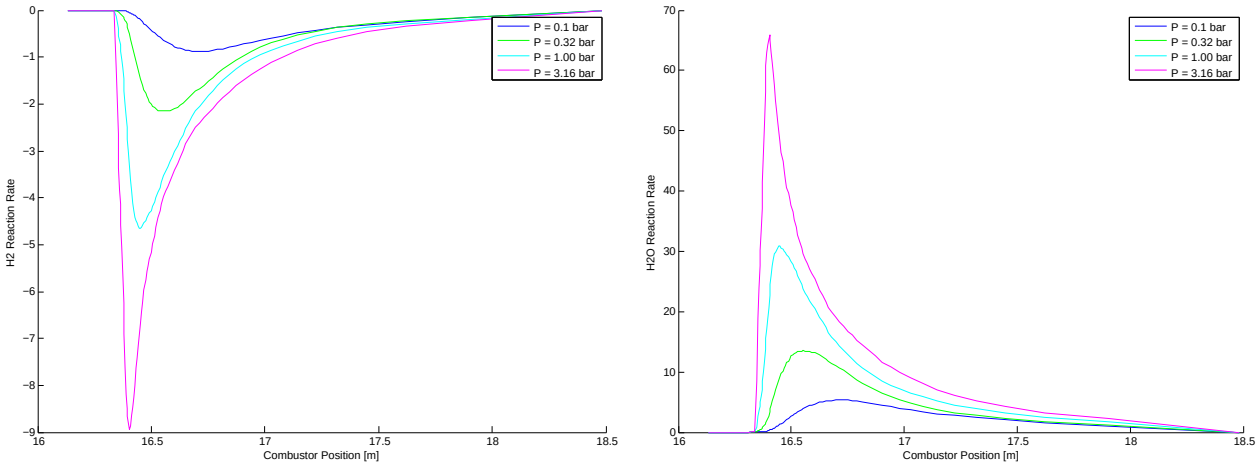

a) Hydrogen H_2 **b) Water** H_2O

Figure 5. Reaction rates of H2 and H2O as a function of the downstream distance (x) in the scramjet combustor

The reaction rate values in Figure 4 were integrated over the transverse (y, z) plane to yield a reaction rate that is only a function of x, the streamwise coordinate. Figure 5 shows the result. The reaction rate of H2 is plotted in Fig. 5a; note that this rate is a negative value. The curve marked p = 3.16 bar is the highest pressure condition and this curve extends downward the farthest. The curve marked p = 0.1 bar has a much smaller magnitude of reaction rate. In Fig. 5b are plots of the reaction rate of H2O; these values are positive. Again, the highest pressure leads to the largest reaction rates, as expected.

Both plots in Fig. 5 show that if the pressure is less than 0.5 bar, the reaction rates are much less than for the higher pressure cases. This confirms the general rule that combustor pressure should be kept at more than 0.5 atm. for proper operation of a hypersonic propulsion system. This requires sufficient compression of the air in the inlet from the ambient pressure up to the desired combustor pressure. Reaction rates of H2O shown in Fig. 7 show a similar trend.

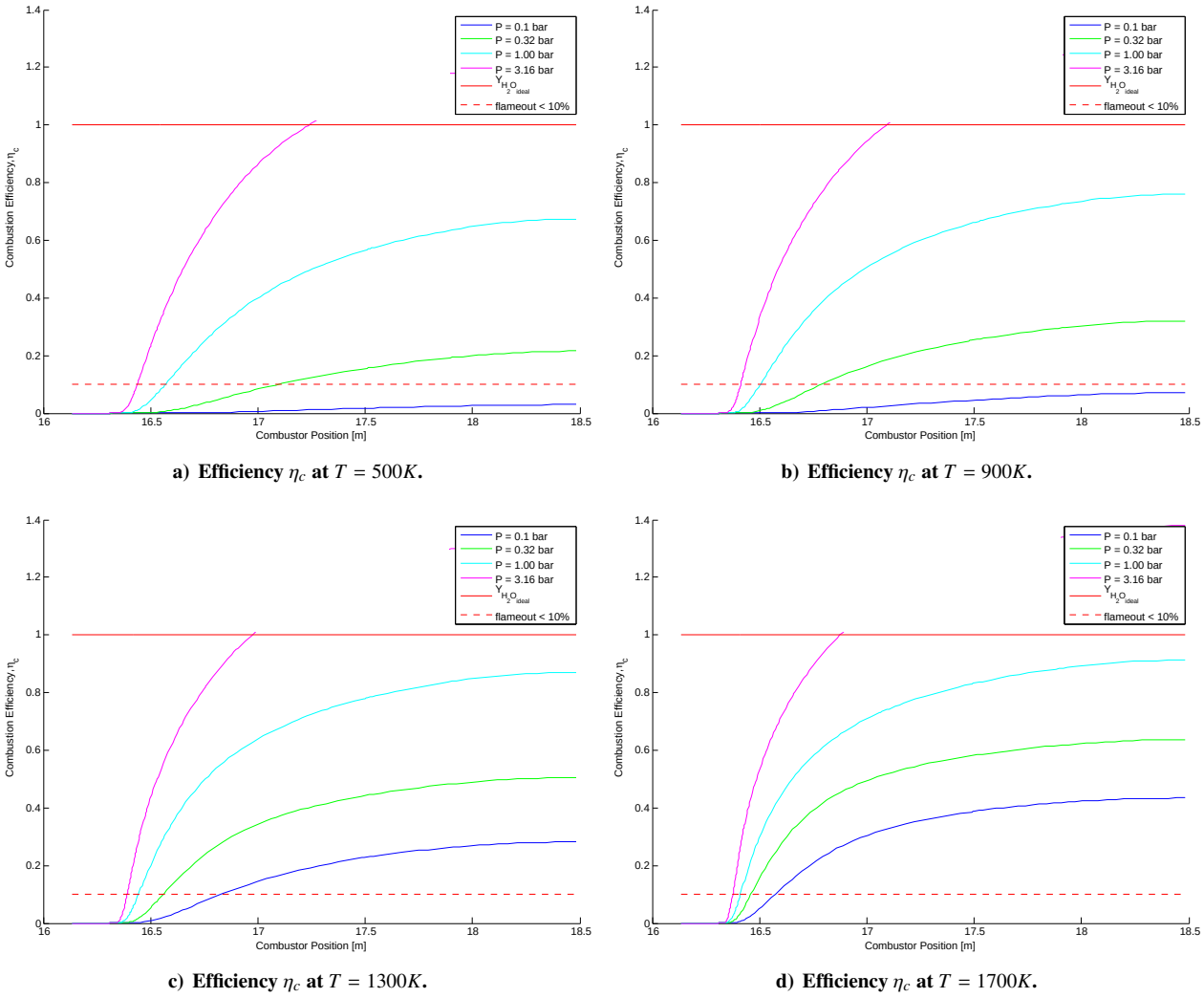

a) Efficiency η_c at $T = 500K$.

b) Efficiency η_c at $T = 900K$.

c) Efficiency η_c at $T = 1300K$.

d) Efficiency η_c at $T = 1700K$.

Figure 6. Combustion efficiency, computed by the MASIV code finite rate chemistry tables

Combustion efficiency was computed using Eq. 20 and using the computed profiles of H2O mass fractions,which are not shown. The resulting plots of combustion efficiency appear in Fig. 6. They increase from zero at the fuel injector to a final value at the end of the combustor (x = 18.5 cm). In some cases the efficiency rises to greater than unity because of gas dissociation, which causes the H2O mass fraction to differ from the undissociated mass fraction. What is seen is that for pressures less than 0.5 atm. in the combustor, a significant fraction of the hydrogen fuel is not consumed to form H2O. The residence time in the combustor is too short for the high speed air flow, which has a velocity of 2,000 m/s.

The dotted line in Fig. 6 is drawn where combustion efficiency has dropped to less than 0.10. There is essentially no burning so this can be defined to be a flameout limit. The lowest pressure condition (p = 0.1 bar) leads to a curve in Fig. 6 that lies below a combustion efficiency of 0.1 at the combustor exit for a combustor entrance temperature of 500 K or 900 K. These conditions provide essentially no thrust. When entrance temperature is raised to 1300 K or 1700 K (Fig. 6c and 6d) then more of the fuel burns even at the lowest pressures.

The MASIV code allows for variations in the number of sidewall fuel port injectors (N). As N is increased in the lateral direction, the same total amount of fuel is injected through more ports, so the fuel injected from each port is smaller. This is a strategy to mix faster and have shorter flames that are fully contained in the combustor. This approach is being used to find the optimum number of fuel ports (N) that provide a combustion efficiency above the desired value of 0.95.

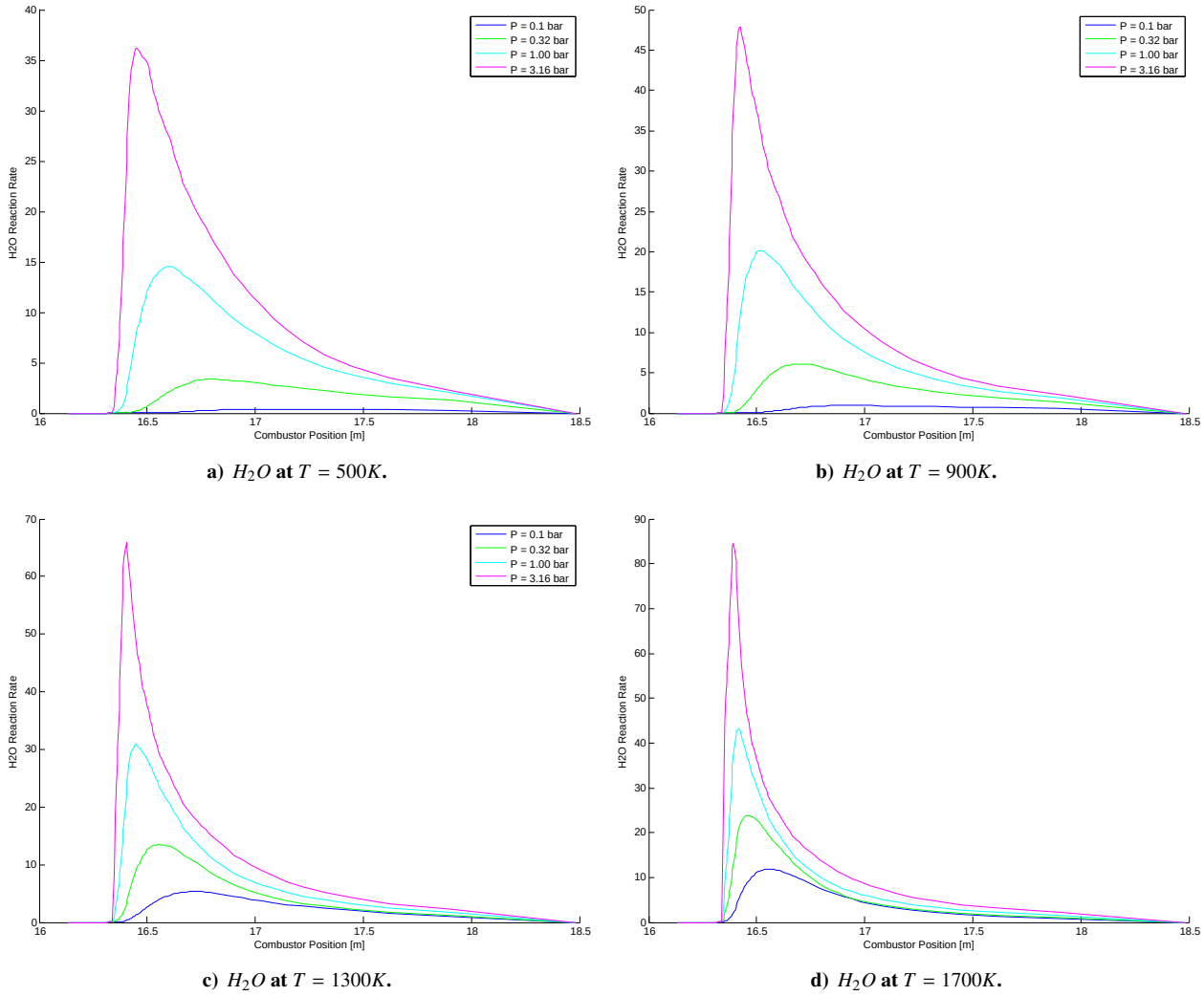

a) H_2O **at** $T = 500K$**.** **b)** H_2O **at** $T = 900K$**.**

c) H_2O **at** $T = 1300K$**.** **d)** H_2O **at** $T = 1700K$**.**

Figure 7. Reaction rates of H2O for various combustor entrance pressures and temperatures.

This research is supported by AFRL as part of the MAX center at the University of Michigan. Dr. Michael Bolender is the contract monitor. The first author is supported by an University of Michigan graduate student fellowship.

References

[1] Bolender, M. a. and Doman, D. B., "Nonlinear Longitudinal Dynamical Model of an Air-Breathing Hypersonic Vehicle," *Journal of Spacecraft and Rockets*, Vol. 44, No. 2, 2007, pp. 374–387.

[2] Parker, J. T., Serrani, A., Yurkovich, S., Bolender, M. a., and Doman, D. B., "Control-Oriented Modeling of an Air-Breathing Hypersonic Vehicle," *Journal of Guidance, Control, and Dynamics*, Vol. 30, No. 3, 2007, pp. 856–869.

[3] Skujins, T., Cesnik, C. E., Oppenheimer, M. W., and Doman, D. B., "Canard-Elevon Interactions on a Hypersonic Vehicle," *Journal of Spacecraft and Rockets*, Vol. 47, No. 1, 2010, pp. 90–100.

[4] Oppenheimer, M. and Doman, D., "A Hypersonic Vehicle Model Developed With Piston Theory," *AIAA Atmospheric Flight Mechanics Conference and Exhibit*, , No. August, 2006.

[5] O'Neill, M. K. L. and Lewis, M. J., "Design tradeoffs on scramjet engine integrated hypersonic waverider vehicles," *Journal of Aircraft*, Vol. 30, No. 6, 1993, pp. 943–952.

[6] Bowcutt, K. G., "Multidisciplinary Optimization of Airbreathing Hypersonic Vehicles," *Journal of Propulsion and Power*, Vol. 17, No. 6, 2001, pp. 1184–1190.

[7] McQuade, P. D., Eberhardt, S., and Livne, E., "CFD-based aerodynamic approximation concepts optimization of a two-dimensional scramjet vehicle," *Journal of Aircraft*, Vol. 32, No. 2, 1995, pp. 262–269.

[8] Mor, M. and Livne, E., "Multidisciplinary Design Optimization of Reentry Vehicles : Trajectory Optimization and Sensitivities," *47th AIAA/ASME/ASCE/AHS/ASC Structures, Structural Dynamics, and Materials Conference*, , No. Paper 2006-1718, 2006, pp. 1–30.

[9] Dalle, D. J., Fotia, M. L., and Driscoll, J. F., "Reduced-Order Modeling of Two-Dimensional Supersonic Flows with Applications to Scramjet Inlets," *Journal of Propulsion and Power*, Vol. 26, No. 3, May 2010, pp. 545–555.

[10] Torrez, S. M., Driscoll, J. F., Ihme, M., and Fotia, M. L., "Reduced-Order Modeling of Turbulent Reacting Flows with Application to Ramjets and Scramjets," *Journal of Propulsion and Power*, Vol. 27, No. 2, March 2011, pp. 371–382.

[11] Torrez, S. M., Dalle, D. J., and Driscoll, J. F., "New Method for Computing Performance of Choked Reacting Flows and Ram-to-Scram Transition," *Journal of Propulsion and Power*, Vol. 29, No. 2, March 2013, pp. 433–445.

[12] Dalle, D. J., Torrez, S. M., and Driscoll, J. F., "Rapid Analysis of Scramjet and Linear Plug Nozzles," *Journal of Propulsion and Power*, Vol. 28, No. 3, 2012, pp. 545–555.

[13] Lumley, J. L., "The structure of inhomogeneous turbulent flows," *Atmospheric turbulence and radio wave propagation*, 1967, pp. 166–178.

[14] Berkooz, G., Holmes, P., and Lumley, J. L., "The Proper Orthogonal Decomposition in the Analysis of Turbulent Flows," *Annual Review of Fluid Mechanics*, Vol. 25, No. 1, 1993, pp. 539–575.

[15] Poje, A. C. and Lumley, J. L., "A model for large-scale structures in turbulent shear flows," *Journal of Fluid Mechanics*, Vol. 285, No. -1, 1995, pp. 349.

[16] Tang, K., Graham, W., and Peraire, J., "Active flow control using a reduced order model and optimum control," *AIAA paper*, , No. June, 1996.

[17] Romanowski, M., "Reduced order unsteady aerodynamic and aeroelastic models using Karhunen-Loeve eigenmodes," *AIAA paper*, 1996, pp. 7–13.

[18] Kim, T., "Frequency-domain Karhunen-Loeve method and its application to linear dynamic systems," *AIAA Journal*, Vol. 36, No. 11, 1998, pp. 2117–2123.

[19] Lucia, D. J., Beran, P. S., and Silva, W. a., "Aeroelastic System Development Using Proper Orthogonal Decomposition and Volterra Theory," *Journal of Aircraft*, Vol. 42, No. 2, 2005, pp. 509–518.

[20] Beran, P. and Pettit, C., "Prediction of nonlinear panel response using proper orthogonal decomposition," *AIAA paper*, , No. c, 2001.

[21] Thomas, J. P., Dowell, E. H., and Hall, K. C., "Three-Dimensional Transonic Aeroelasticity Using Proper Orthogonal Decomposition-Based Reduced-Order Models," *Journal of Aircraft*, Vol. 40, No. 3, 2003, pp. 544–551.

[22] Kim, T., Hong, M., Bhatia, K. G., and Sengupta, G., "Aeroelastic Model Reduction for Affordable Computational Fluid Dynamics-Based Flutter Analysis," *AIAA Journal*, Vol. 43, No. 12, 2005, pp. 2487–2495.

[23] Cao, Y., Zhu, J., Navon, I. M., and Luo, Z., "A reduced-order approach to four-dimensional variational data assimilation using proper orthogonal decomposition," *International Journal for Numerical Methods in Fluids*, Vol. 53, No. 10, April 2007, pp. 1571–1583.

[24] Vanquickenborne, L. and Tiggelen, A. V., “The stabilization mechanism of lifted diffusion flames,” Combustion and Flame,1966, pp. 59–69.
[25] KALGHATGI, G. T., “Blow-Out Stability of Gaseous Jet Diffusion Flames. Part I: In Still Air,” Combustion Science and Technology, Vol. 26, No. 5-6, Oct. 1981, pp. 233–239.
[26] KALGHATGI, G. T., “Lift-off Heights and Visible Lengths of Vertical Turbulent Jet Diffusion Flames in Still Air,” Combustion Science and Technology, Vol. 41, No. 1-2, Sept. 1984, pp. 17–29.
[27] Hall, K., Thomas, J., and Dowell, E., “Proper Orthogonal Decomposition Technique for Transonic Unsteady Aerodynamic Flows,” AIAA journal, Vol. 38, No. 10, 2000.
[28] Rathinam, M. and Petzold, L. R., “A New Look at Proper Orthogonal Decomposition,” SIAM Journal on Numerical Analysis, Vol. 41, No. 5, Jan. 2003, pp. 1893–1925.
[29] Strang, G., “Linear Algebra and Its Applications,” 1988.
[30] Dahm, W. and Mayman, A., “Blowout limits of turbulent jet diffusion flames for arbitrary source conditions,” AIAA journal, Vol. 28, No. 7, 1990, pp. 1157–1162.
[31] Driscoll, J. F. and Rasmussen, C. C., “Correlation and Analysis of Blowout Limits of Flames in High-Speed Airflows,” Journal of Propulsion and Power, Vol. 21, No. 6, Nov. 2005, pp. 1035–1044.
[32] Micka, D. J. and Driscoll, J. F., “Stratified jet flames in a heated (1390K) air cross-flow with autoignition,” Combustion and Flame, Vol. 159, No. 3, March 2012, pp. 1205–1214.
[33] Rasmussen, C. C., Driscoll, J. F., Hsu, K.-Y., Donbar, J. M., Gruber, M. R., and Carter, C. D., “Stability limits of cavity stabilized flames in supersonic flow,” Proceedings of the Combustion Institute, Vol. 30, No. 2, Jan. 2005, pp. 2825–2833.

VII. Appendix

A. Preliminary Hydrogen Combustion Analysis

Plot of combustion efficiency against cross-flow velocity.

Stoichiometric hydrogen combustion reaction (simple):

$$H_2 + \frac{1}{2}\left(O_2 + \frac{79}{21}N_2\right) \longrightarrow H_2O + \frac{1}{2}\left(\frac{79}{21}\right)N_2 \tag{24}$$

Fuel-to-oxidizer ratio, stoichiometric:

$$FAR_{sto} = \frac{1 \text{ mol } H_2}{1/2 \text{ mol air}} = \frac{1(2 \text{ g/mol})}{1/2\left(32 \text{ g/mol} + \frac{79}{21}(28) \text{ g/mol}\right)} = 0.0291 \tag{25}$$

Non-stoichiometric reaction:

$$\text{Fuel-lean: } H_2 + (n)\frac{1}{2}\left(O_2 + \frac{79}{21}N_2\right) \longrightarrow H_2O + (n-1)\frac{1}{2}O_2 + (n)\frac{1}{2}\left(\frac{79}{21}\right)N_2 \tag{26}$$

Fuel-to-oxidizer ratio, non-stoichiometric:

$$FAR = \frac{1 \text{ mol } H_2}{(n)1/2 \text{ mol air}} = \frac{1(2 \text{ g/mol})}{(n)1/2\left(32 \text{ g/mol} + \frac{79}{21}(28) \text{ g/mol}\right)} = \frac{0.0291}{n} \tag{27}$$

Equivalence ratio ϕ is defined as the ratio of the fuel-to-oxidizer ratio to its stoichiometric counterpart, or:

$$\phi = \frac{FAR}{FAR_{sto}} = 1/n \tag{28}$$

Substituting back into our (non-stoichiometric) reaction, we have:

$$H_2 + \frac{1}{2\phi}\left(O_2 + \frac{79}{21}N_2\right) \longrightarrow H_2O + (\frac{1}{\phi} - 1)\frac{1}{2}O_2 + \frac{1}{2\phi}\left(\frac{79}{21}\right)N_2 \tag{29}$$

In determining combustion efficiency, we look at the mass fraction of H_2O of the combustion products. For a given equivalence ratio, our "ideal" H_2O mass fraction (i.e. where all the fuel is burned) is:

$$Y_{H_2O_{ideal}} = \frac{m_{H_2O}}{m_{\text{total}}} = \frac{(18) \text{ g/mol}}{(18) \text{ g/mol} + (\frac{1}{\phi} - 1)\frac{1}{2}(32) \text{ g/mol} + (\frac{1}{2\phi})\frac{79}{21}(28) \text{ g/mol}} \tag{30}$$

Setting the equivalence ratio $\phi = 0.3$:

$$Y_{H_2O_{ideal}} = 0.078 \tag{31}$$

Setting the equivalence ratio $\phi = 1$:

$$Y_{H_2O_{ideal}} = 0.255 \tag{32}$$

For an equivalence ratio of $\phi = 1$, the ratio of mass flow rates of fuel and air is the same as the stoichiometric fuel-to-oxidizer ratio:

$$\frac{\dot{m}_f}{\dot{m}_a} = FAR_{sto} = 0.0291 \tag{33}$$